Taylor & Francis
Taylor & Francis Group

Science and Technology of Advanced Materials: Methods

ISSN: (Print) (Online) Journal homepage: www.tandfonline.com/journals/tstm20

Automated microscopy image analysis of sintered cBN materials

Dmitry S. Bulgarevich, Moe Sakaguchi, Nobuyasu Nita & Masahiko Demura

To cite this article: Dmitry S. Bulgarevich, Moe Sakaguchi, Nobuyasu Nita & Masahiko Demura (2024) Automated microscopy image analysis of sintered cBN materials, Science and Technology of Advanced Materials: Methods, 4:1, 2423599, DOI: 10.1080/27660400.2024.2423599

To link to this article: https://doi.org/10.1080/27660400.2024.2423599

Published online: 14 Nov 2024.

SCIENCE AND TECHNOLOGY OF ADVANCED MATERIALS: METHODS
2024, VOL. 4, NO. 1, 2423599
https://doi.org/10.1080/27660400.2024.2423599

Automated microscopy image analysis of sintered cBN materials

Dmitry S. Bulgarevich[a], Moe Sakaguchi[b], Nobuyasu Nita[b] and Masahiko Demura[c]

[a]Research Center for Structural Materials, National Institute for Materials Science, Tsukuba, Japan; [b]Innovation Center, Mitsubishi Materials Corporation, Naka, Japan; [c]Research Network and Facility Service Division, National Institute for Materials Science, Tsukuba, Japan

ABSTRACT

Two protocols for multistep grain segmentation and analysis workflow in optical microscopy images of cubic boron nitride materials were developed and compared. One is based on statistical region merging and second one on morphological segmentation of grains without high contrast borders. Judging from corresponding manual image segmentation by expert, the second method gave more accurate grain boundaries and better statistical correspondence. Then, using the morphological segmentation method and incorporating of parameter optimization into it, a grain analysis workflow was established. Deviations from the correct answer (expert segmentation) were quantified based on five geometric statistical indices, and these deviations were added together to define the overall error. Cross-validation confirmed that the morphological segmentation workflow reproduces the expert segmentation with smaller 9.4% margin of error compared to 23.9% with statistical region merging one. The automated grain segmentation of such challenging materials with high throughput image analysis is an important help for industrial development of new milling tools.

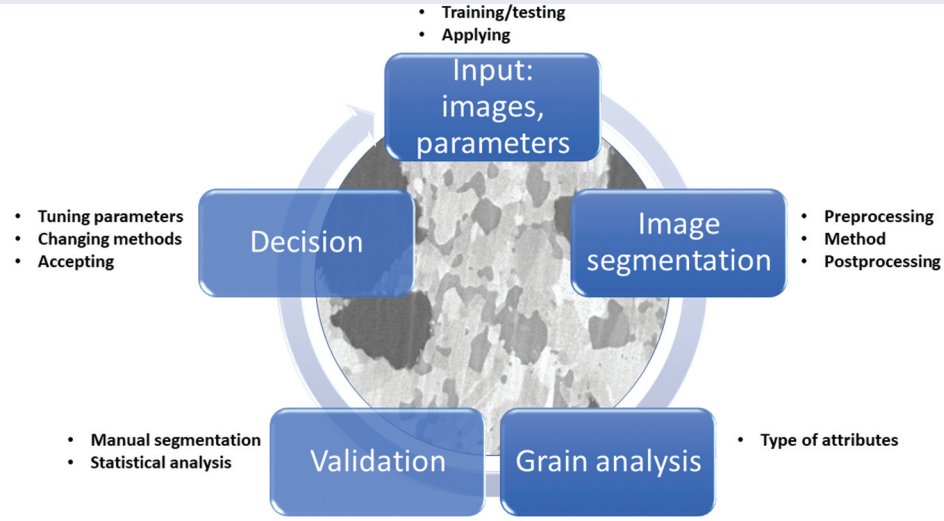

General Outline of Automatic Image Segmentation and Analysis for Grains without Clear Boundaries

IMPACT STATEMENT

For grains without clear boarders, the unique, automated, and fast SEM image analysis protocol is reported for sintered industrially important cBN materials with segmentation quality close to expert level one.

ARTICLE HISTORY
Received 28 December 2023
Revised 23 September 2024
Accepted 27 October 2024

KEYWORDS
Metallurgy; image analysis; microstructures; optical microscopy; grain recognition; cBN sintered compacts

1. Introduction

Grain analysis is one of the basic techniques in metallurgy since statistical grain size and morphology greatly determine the materials mechanical properties (mechanical strength, toughness, fracture resistance, creep, etc.) and can be subsequently used in various theoretical and computational mathematical modeling approaches [1]. The present target material, cBN sintered compacts, is one of the typical examples. The cBN sintered compacts are widely used as cutting tools of ferrous materials [2,3], and it is important to understand the wear mechanism of edge damage for flank wear, rake wear, and edge chipping. For understanding these complicated damage phenomena, the quantitative information on the microstructure such as grain size and morphology of the cBN matrix phase is crucial and fundamental ones.

CONTACT Dmitry S. Bulgarevich BULGAREVICH.Dmitry@nims.go.jp Additive Manufacturing Group, Research Center for Structural Materials (RCSM), National Institute for Materials Science (NIMS), 1-2-1 Sengen, Tsukuba, Ibaraki 305-0047 JAPAN

Most of the data for such studies come from optical- or/and electron-microscopy imaging techniques. Owing to large volume of associated image data for accurate statistical analysis, the traditional manual examination could be significantly slow. Nowadays, industrial microscopes are often bounded with corresponding grain analysis software to automate such task [4–7] in large area imaging. Nevertheless, grain segmentation with low contrast or incomplete borders remains to be a challenge, and it is typically conducted manually by expert in the field of particular metallurgical materials. It should be straightforward to use the electron backscattered diffraction method in scanning electron microscopy (SEM-EBSD), which provides crystallographic orientation useful for grain segmentation. The SEM-EBSD measurements, however, require so long time that it is impractical to acquire a large amount of data; in addition, the method is limited to electron microscopy.

In past decades, various image segmentation algorithms of different complexity were developed for diverse fields [8]. The basic image segmentation and processing tools used in our previously reported works on different metallurgical materials [9,10] were originally built for computer vision [11], biology [12], and concrete technology [13] applications. By using different basic image segmentation and processing analysis tools as well as statistical analysis in this work, we here develop the automated grain analysis protocols for cBN sintered compacts that exhibit weak-contrast grain structure with no clear boundary in the SEM images. The cBN sintered compacts have a complicated multi-phase structure that can be regarded as one of the most difficult microstructures for the grain segmentation task. Thus, we expect that the developed protocols can be applied to a wide range of multiphase, polycrystalline materials.

2. Experimental details

The cBN compacts were made by sintering of the cBN powder with ceramics binder, and they exhibited the microstructure consisting of cBN matrix, fine TiN binder, and highly dispersed nano-Al_2O_3 particles. SEM observations were performed by using Zeiss Ultra 55: Carl Zeiss Microscopy GmbH (Germany) with a multi-detector system. Auger electron spectroscopy (AES) was conducted by using PHI-700: ULVAC-PHI, Inc. (Japan) apparatuses to obtain the elemental map of sintered materials.

Automated image analysis protocols were developed in the form of executable macros by using an open-source FIJI software package [14–17] with particular plugins referenced in the text below.

3. Results and discussion

Figure 1 demonstrates the typical problem of using some simple edge detection filtering on the SEM image of the cBN matrix shown in Figure 1(a). In Figure 1(b), we used the Gaussian Blur filter with followed brightness and contrast adjustments before applying the Canny Edge detection filter [18] in Figure 1(c). Then, the connected regions were found in Figure 1(d) [19], and the image was converted into the binary one in Figure 1(e). Finally, Figure 1(f) demonstrates the segmented grains. At this stage, at least five independent parameters already need to be adjusted to get Figure 1(f). However, the grain borders are too thick in Figure 1(e) and require an extra tuning with Erode or threshold filtering. Moreover, many grain borders are not closed even in this case, and grains have many debris. For thinner borders with tuned Canny Edge filtering, this problem became even more severe. This demands an additional set of image

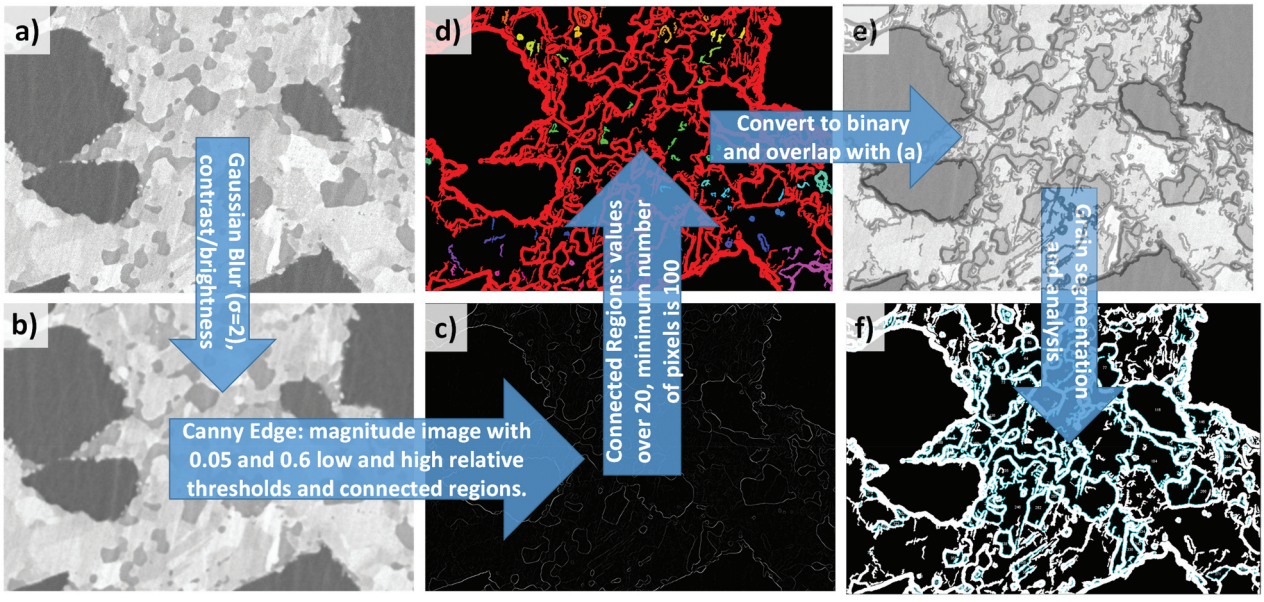

Figure 1. The typical results with edge detector filters in borderless-grain segmentation workflow (see text for more details).

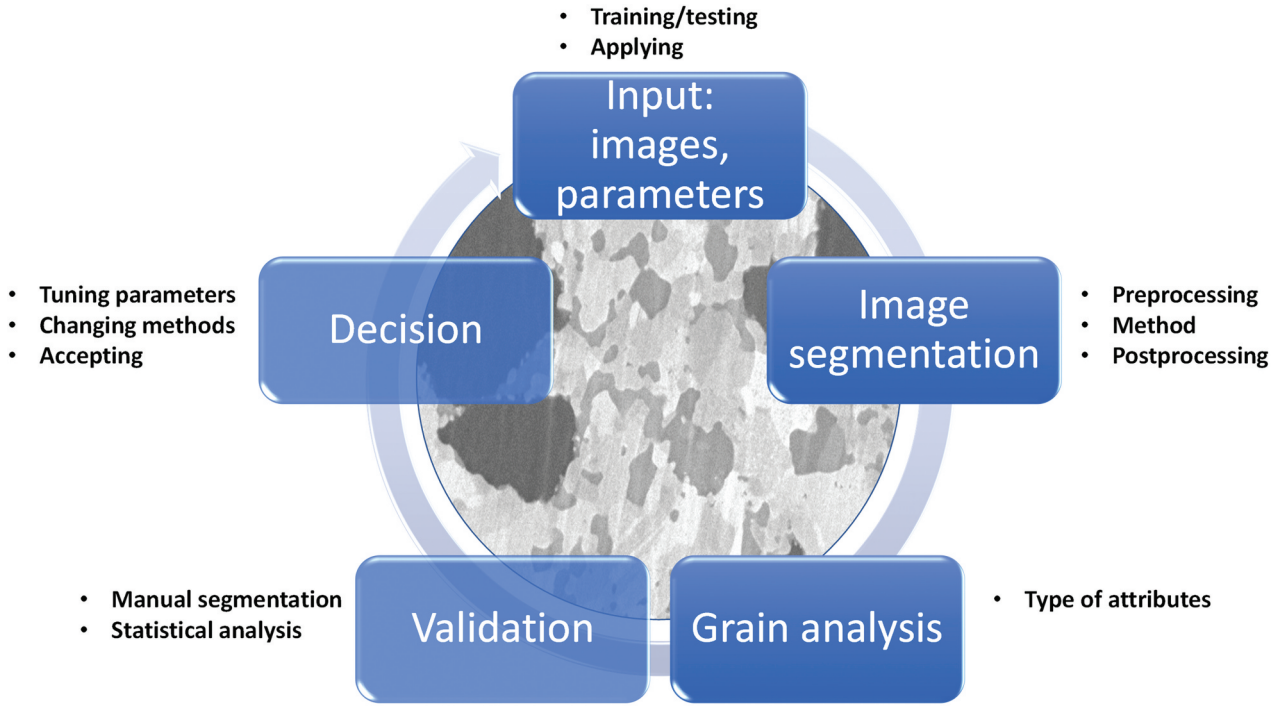

Figure 2. The general outline of the developed grain analysis protocol for cBN compacts from their SEM images.

processing, so the grain analysis from Figure 1(f) is not correct at this stage. In summary, the well-known image analysis techniques for grains with well-defined borders simply do not work for our samples due to the cumbersome protocols with large hyper-parameter search space, but mediocre outcome. The same problem is with other simple edge image filters or/and thresholds.

In this regard, Figure 2 shows the general outline of developed grain analysis workflow for cBN compacts. Two different image segmentation algorithms with sets of corresponding parameters were tested and compared in the same images as discussed below.

3.1. Grain analysis workflow with statistical region merging segmentation protocol in its core

Statistical region merging (SRM) segmentation is a fast and robust algorithm to segment an image into regions of similar grayscale intensity [11,20]. With SRM, the initial regions are set for pixels with homogeneous properties which are later grew/merge depending on statistical test at the local spatial level. The merging predicate ($\mathcal{P}$) for grayscale images is in Equation (1):

$$P(R,R') = \begin{cases} \text{true } if \left|\bar{R}' - \bar{R}\right| < \sqrt{b^2(R) + b^2(R')} \\ \text{false } otherwise \end{cases}, \tag{1}$$

with $b(R) = g\sqrt{(1/(2Q|R|))\left(ln\left(\left|\mathcal{R}_{|R|}\right|\right)/\delta\right)}$ where $\sqrt{b^2(R) + b^2(R')}$ is a merging threshold; $|.|$ is the cardinal notation for size of sets of variables; R, R' and $\bar{R}$, $\bar{R}'$ are the couple of regions of observed image (I) with $|I|$ pixels and their observed averages of corresponding grayscale bands; $\mathcal{R}$ *is* the set of regions with R pixels; $g = 256$ is from the set $\{1, 2, \ldots, g\}$ of pixel values; Q is the set of the independent random variables bounded by g/Q domain with any possible sum of outcomes of Q belonging to $\{1, 2, \ldots, g\}$, i.e. it is the statistical complexity parameter of theoretical (expected) image I^* after segmentation of I; and $0 < \delta \leq 1$ with probability $\delta = 1/\left(6|I|^2\right)$ from *big O-h* notation is related to the quantitative upper bound of error with respect to optimal segmentation. The merging order prioritizes that all tests inside each of the two true regions have previously occurred. Therefore, the only tuning parameter in SRM implementation is Q ranging through the g values which control the coarseness of the segmentation. Note that used SRM implementation [11] works only with 8-bit images, i.e. with $1 \leq Q \leq 256$, $\Delta Q = 1$.

To improve the grain shape/size recognition for connected grain clusters after SRM segmentation, the enhanced watershed algorithm (EWA) is additionally applied which can tolerate concavities in grain clusters up to a certain degree before separation [13,21]. It includes the automatic binary thresholding of the original image based on its histogram analysis and subsequently Euclidean distance transform $D(x, y, z)$ on resulted binary image. The interconnected particles p_{i1} and p_{i2} were separated from each other by successive particle p_j erosion to allow splitting at the concave necks by Equation (2):

$$D_j(x,y,z) = \begin{cases} 1, \forall D(x,y,z) > d_j \\ 0, \text{ otherwise} \end{cases}, \quad (2)$$

where d_j is eroding distance with respect to radii of maximum distances from interior of p_{i1} and p_{i2} to the corresponding surface boundaries by satisfying the constrains $c_{i1,j}(k) = \left(d_j < kr_{p_{i1}}\right)$ and $c_{i2,j}(k) = \left(d_j < kr_{p_{i2}}\right)$. Whether an object with a given concavity was effectively split into two objects depend on a user predefined proportionality constant $(0 \leq k \leq 1)$. For $k = 0$, the particles were not divided, whereas for $k = 1$, the particles are split at any concavity.

As a result, the outline of SRM protocol shown in Figure 3(a–f) involves following: 1) the preprocessing with Gaussian filtering having width parameter (σ) on original image (a), 2) applying the SRM on filtered image (b), 3) adjusting the grain separation in SRM processed image (c) with EWA, 4) overlaying the EWA processed and original images (d) and (a) for manual comparison (e), and 5) statistical analysis of geometrical characteristics of the segmented grains (f). Therefore, in the SRM protocol, there are three tunable parameters to get the correspondence with manual expert-level segmentation: σ, Q, and k. The list of geometrical characteristics extracted from developed image segmentation and analysis protocols are listed in Table 1.

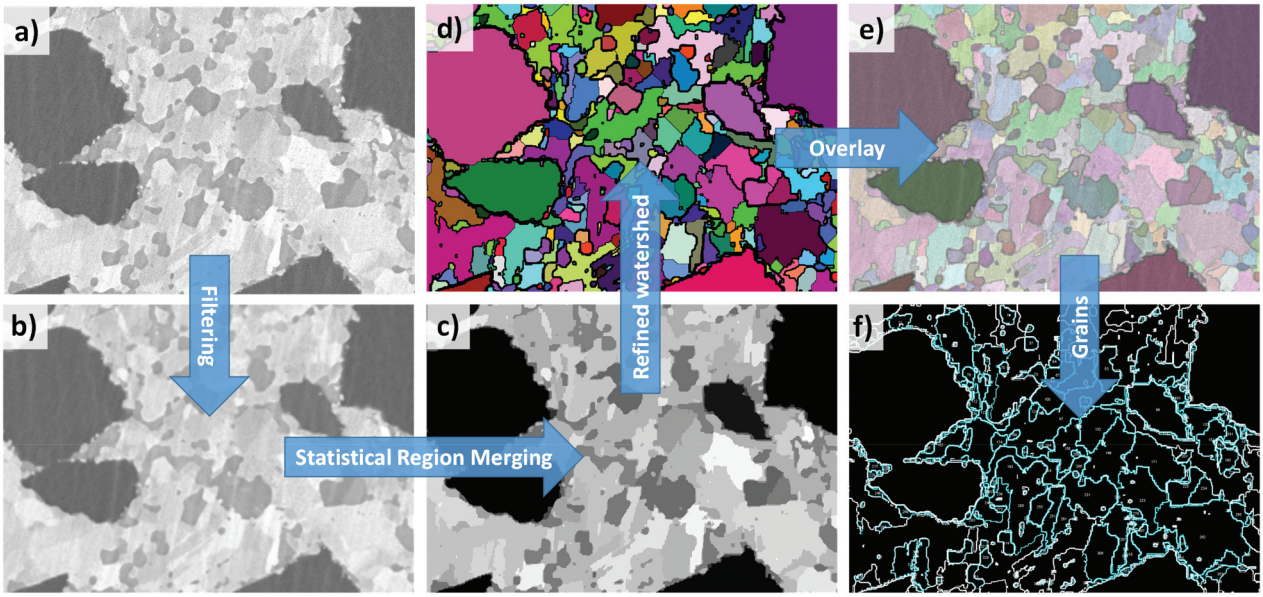

Figure 3. Grain segmentation workflow with the statistical region merging (SRM) protocol where the main adjustable parameters are σ, Q, and k (see text for more details).

Table 1. Geometrical statistical parameters for characterization of the grains in Figures 3(f) and **5(e).**

№	Attribute	Definition	Comment
1	Count	Black objects	Absolute value
2	Total Area	Black objects	Absolute value
3	Size	Black objects	Individual and statistical values
4	%Area	Black objects	Absolute value
7	Perimeter	Black objects	Individual and statistical values
8	Major	Axis of fitted ellipse into black object with same area and second order central moments	Individual and statistical values
9	Minor	Axis of fitted ellipse into black object with same area and second order central moments	Individual and statistical values
10	Angle	Angle between the fitted ellipse axis of the black object and a line parallel to the X-axis of the image	Individual and statistical values
11	Circularity	Black objects, $4\pi \times [Size]/[Perimeter]$	Individual and statistical values
12	Solidity	Black objects, $4\pi \times [Size]/[Convexarea]$	Individual and statistical values
13	Feret	Maximum caliper of black objects	Individual and statistical values
17	MinFeret	Minimum caliper of black objects	Individual and statistical values
19	Aspect ratio	$[Major]/[Minor]$	Individual and statistical values
20	Density	$[Count]/[TotalArea]$	Absolute value
21	Surface Density	$[Count]/[\mu m^2]$	Absolute value

3.2. Grain analysis workflow with morphological segmentation protocol in its core

Compared to classical watershed transformation algorithms of I pixel brightness to a height/depth in a topographic map with lines along the tops of the ridges [22], the morphological segmentation (MS) of I can significantly avoid over-segmentation of structured surface by removing of non-significant minima with the h-minima transform method [12,23,24] by Equation (3):

$$H_{min_H}(f) = R_{\varepsilon f}(f + H), \tag{3}$$

where $H = N * Z$ is the height threshold value (non-negative scalar); Z is the maximum height from mean plane; N is the percentage from maximum height (usually, ~5-20%); and $R_{\varepsilon f}$ is the geodesic reconstruction by erosion of marker function (f) which increases by H. As a result, the significant minima remain, but with increased heights and sizes, while the number of regional minima decreases.

Figure 4(a–e) outlines the MS-based protocol: 1) the preprocessing with Gaussian filtering on original image (a) with width parameter (σ), 2) applying the MS on filtered image (b), 3) overlaying of the MS processed and original images (c) and (a) for manual comparison (d), and 4) statistical analysis of geometrical characteristics of the segmented grains (e). As a result, there are also three tunable parameters in the MS protocol to get the correspondence with manual expert-level segmentation: σ, the gradient radius for dilation and erosion in pixels for watershed transformation (GR), and tolerance of intensity (Tol) for the search of regional minima by removing the non-significant ones.

3.3. Workflow comparisions with manual segmentations by expert

Figure 5 compares the manual segmentation by expert and results by the SRM protocol in terms of appearance and grain distribution together with the comparison of median grain size values ($Feret_{D50}$). A closer look at Figure 5(b) shows that the SRM protocol has a tendency to segment small island-like grains inside gains, and most of the island-like grains segmented were detected by error, not real ones. On the other hand, comparing Figures 5(b) with Figures 3(a,b), there were some cases where grain boundaries that should have been segmented were not detected. In total, the grain distribution obtained by the SRM segmentation was far from that obtained from the expert segmentation, and the $Feret_{D50}$ was overestimated by more than 10% (see Figure 5(c,d)).

Figure 6 compares the manual segmentation by expert and results by the MS protocol in terms of appearance and grain distribution together with the comparison of median grain size values. The segmentation by the MS protocol showed no island-like grains as seen in the SRM protocol, and the interior of the grains was clean. Comparing Figures 6(a,b), the overall segmentation appeared to reproduce the expert's segmentation well. In fact, the grain distribution obtained by the MS segmentation reproduces well the one obtained from the expert segmentation, and $Feret_{D50}$ was in excellent agreement (see Figure 6(c,d)).

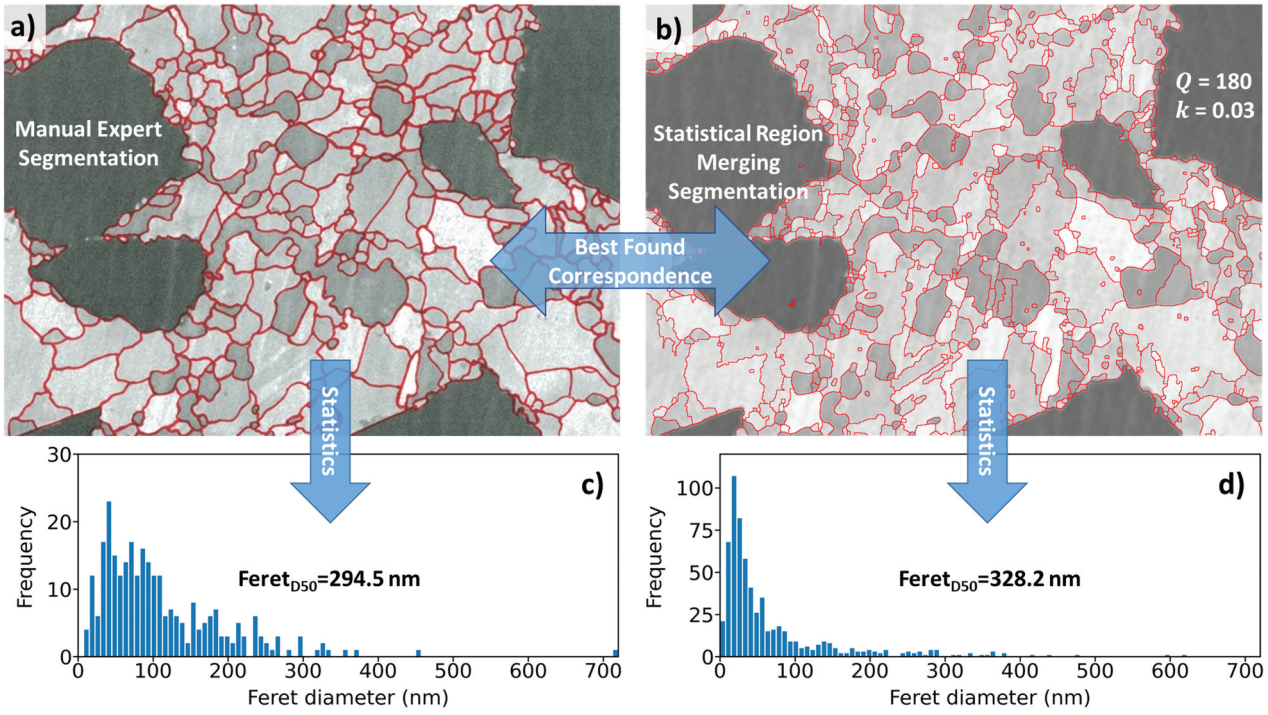

Figure 4. An example of expert validation (a) and (c) for the grain segmentation by the SRM protocol (b) and (d).

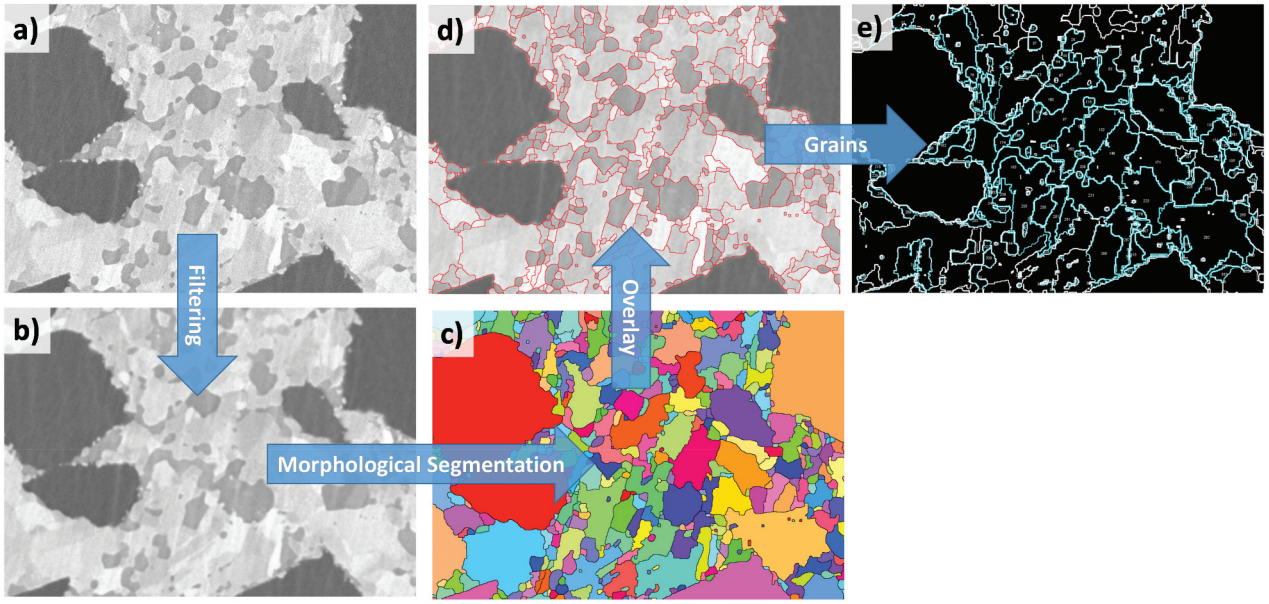

Figure 5. Grain segmentation workflow with the morphological segmentation (MS) protocol where the main adjustable parameters are σ, *GR*, and *Tol* (see text for more details).

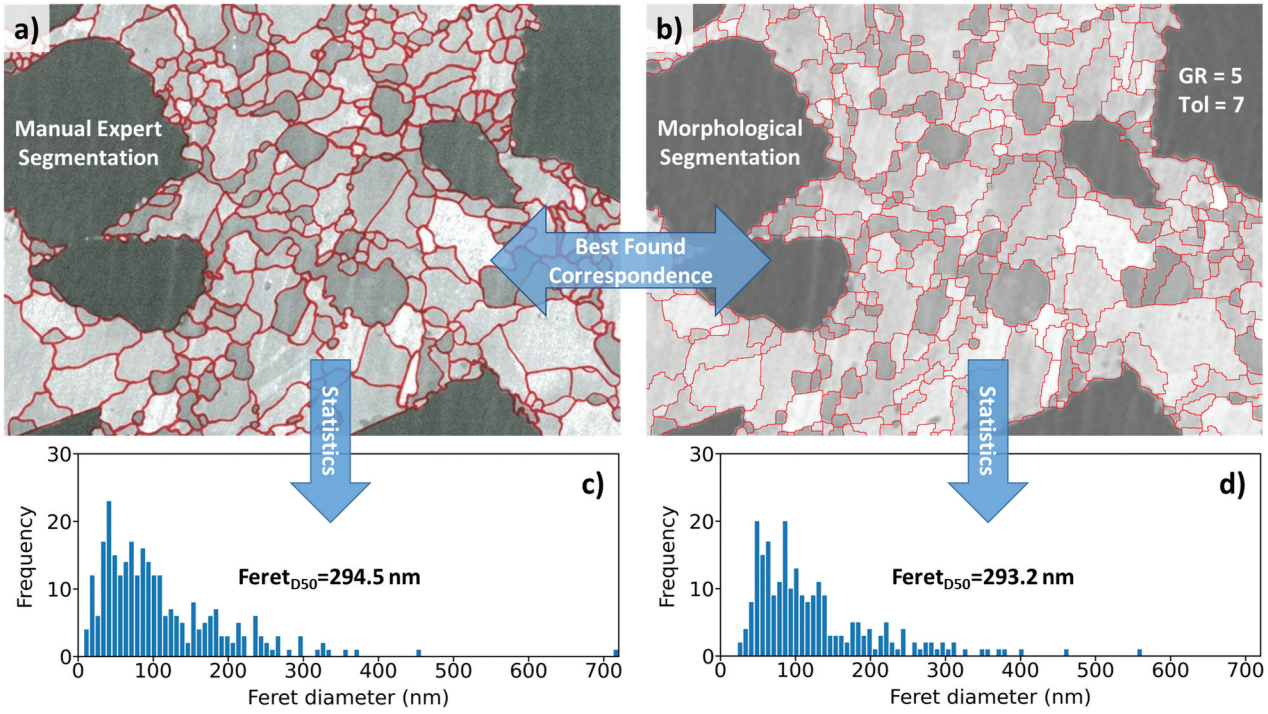

Figure 6. An example of expert validation (a) and (c) for the grain segmentation by the MS protocol (b) and (d).

From the comparisons with the expert segmentation shown in Figures 5 and 6, it was concluded that the MS protocol generally led to the more accurate appearance and grain distribution than the SRM protocol. It should also be noted that the MS protocol required less computational cost than the SRM protocol. Then, in the subsequent sub-sections, we examined the workflows to optimize the parameters in more detail for both protocols.

3.4. Learning the best segmentation parameter set for the constructed protocol based on an expert segmentation

As described above, the incorporated MS protocol contains the σ, *GR*, and *Tol* parameters. These parameters in MS were trained to reproduce as close as possible the segmentation by experts. In detail, we compared the statistics obtained by the expert segmentation with those obtained by the automatic

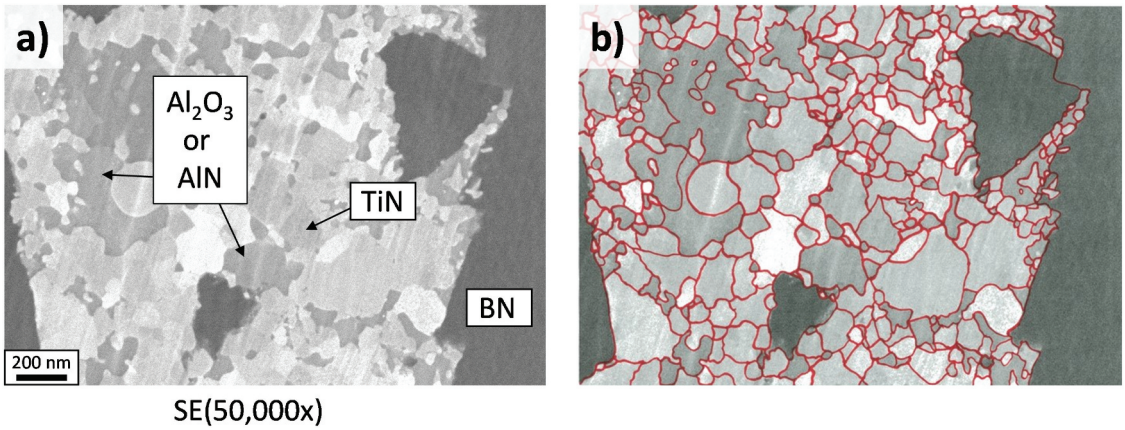

Figure 7. One of the SEM images with indicated phases (a) and segmented by an expert (b) for learning of optimal parameter set in grain segmentation workflow/protocol with morphological segmentation in its core (see text for more details).

analysis and learned theσ, *GR*, and *Tol* values which reproduced the minimal statistical difference from expert segmentation. As an example, one of the training SEM images used for learning is shown in Figure 7(a). At × 50,000 magnification, the crystal grains of the cBN matrix can be clearly recognized but they have no clear borders. Note that pixels in BN regions have the lowest brightness followed by Al_2O_3 regions. Depending on the imaging conditions, the brightness of the TiN pixels is close to that of Al_2O_3, making it difficult to distinguish them with optical microscopy alone. Three of such SEM images ($j = 1$, 2, 3) with the same magnification as in Figure 7(a) were used for training in this study. The outlines of the expert segmentations on one of them are overlaid in Figure 7(b).

The five ($i = 1, 2, \ldots, 5$) statistical values were used to quantitatively evaluate the correspondence with expert segmentation. That is, they were the mean, median, and the standard deviation of the Feret diameter which is the diameter of the spheroid having the same area of a grain (see Table 1), *D*50, and the number of grains. Here, the *D*50 value is the Feret diameter with which or less the total areas of the grains reaches 50% of the total area of all the grains. The error of automated segmentation against expert segmentation, f^j_{hkl}, for a specific image, *j*, and a parameter set, *h*:σ, *k*:*GR*, *l*:*Tol*, is defined by Equation (4):

$$f^j_{hkl} = \frac{\sum_i \left|1 - \frac{C_i}{H_i}\right|}{\sum_i i} \times 100\%, \tag{4}$$

where *i* means a kind of the statistic values; C_i and H_i are the values of *i* obtained from the automated segmentation and the expert segmentation, respectively. Each C_i statistics is normalized by the corresponding expert segmentation value H_i, and thus, the error f^j_{hkl} accounts equally for each kind of the statistics values. Then, the average value of the error $\overline{f^j_{hkl}}$ for all the SEM images used for training is the cost function, F_{hkl} as defined by Equation (5):

$$F_{hkl} = \frac{\sum_j f^j_{hkl}}{\sum_j j}. \tag{5}$$

The best parameter set values $\widehat{h:\sigma}, \widehat{k:GR}, \widehat{l:Tol}$ were obtained by minimizing F_{hkl} with grid search, as expressed by with Equation (6):

$$\hat{h}, \hat{k}, \hat{l} = \arg\min F_{hkl}. \tag{6}$$

The corresponding search ranges for parameter set values were as follows:

$$0 \le h \le 3,$$
$$2 \le k \le 5, \tag{7}$$
$$2 \le l \le 14,$$

with $\Delta h = \Delta k = \Delta l = 1$. As a result, the F_{hkl} variations within the parameter set values are shown in Figure 8. As it can be seen in Figure 8(b), the minimum value of $F_{hkl} = 8.1\%$ was with $h{:}\sigma = 1$, $k{:}GR = 4$, and $l{:}Tol = 9$ parameter set.

For SRM protocol in Figures 9(a,b), the corresponding grid search ranges for parameter set values were as follows:

$$0 \le h \le 3,$$
$$0 \le k \le 1, \tag{8}$$
$$20 \le l \le 256,$$

with $\Delta h = 1$, $\Delta k = 0.1$, $\Delta l = 2$. The minimum value of $F_{hkl} = 17.1\%$ with $\widehat{h:\sigma} = 2, \widehat{k:k} = 0, \widehat{l:Q} = 228$ parameter set was found (see Figure 9(a)). It was more than two times higher compared to the one with MS protocol.

Here, it should be stressed that the grid search method was adequate due to the presence of only

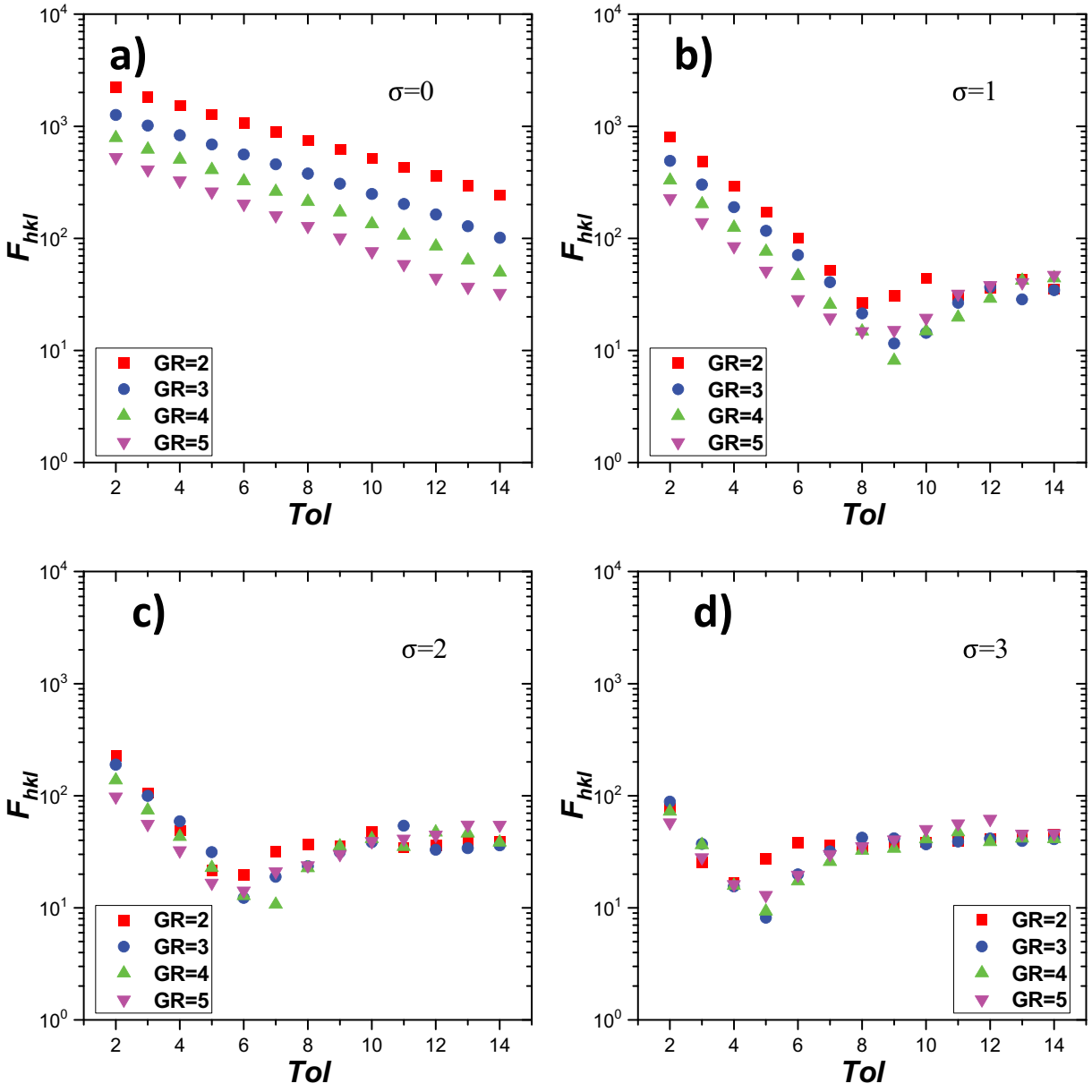

Figure 8. The plots of cost function values with variable parameters in the morphological segmentation protocol (see text for more details).

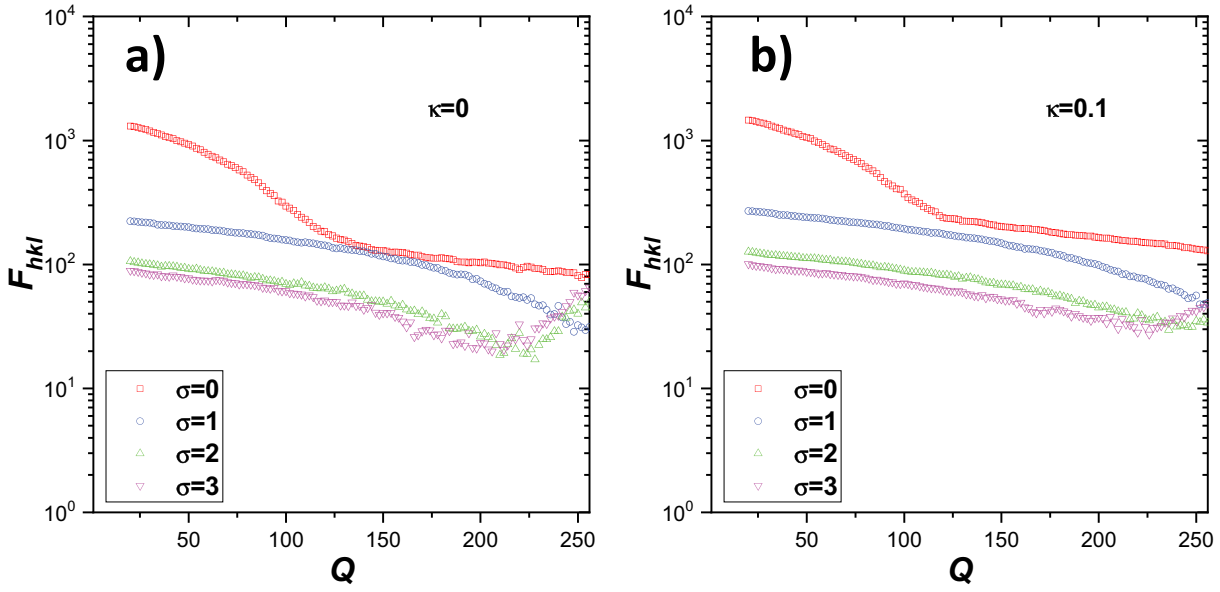

Figure 9. The plots of cost function values with variable parameters in the statistical region merging the segmentation protocol (see text for more details).

three parameters in each protocol and the smooth/simple shape of F_{hkl} as seen in Figures 8 and 9. This is an important advantage of the developed protocols, especially the MS one.

3.5. Leave-one-out cross-validation

We also evaluated the MS-based protocol performance by using the leave-one-out cross-validation. In this method, one of the j images is taken for performance evaluation by Equation (4) with corresponding parameter set learned from $j-1$ images as described above by Equations (4)–(7). Such a procedure was repeated for j number of SEM images, and $F_{hkl}\cong 9.4\%$ was obtained by Equation (5) as the cross-validation value. In the case of SRM protocol, such cross-validation gave $F_{hkl}\cong 23.9\%$ which was again more than two times higher than with MS protocol.

4. Conclusions

In order to establish the automated segmentation for the highly complex microstructures of cBN sintered compacts, we closely examined the two segmentation protocols: SRM and the MS. The comparison with the expert segmentation showed that the MS protocol reproduced the expert segmentation better in terms of appearance and grain distribution. To confirm this, we established the method to optimize the protocol parameters by minimizing the error based on statistics with five values from Feret diameter distribution: mean, median, standard deviation, and D50. Indeed, the cross-validation showed that the MS workflow reproduced the expert's results with minimal 9.4% error. After finding the optimal parameters with grid search method and understanding of the associated analysis error, the MS workflow can be used in a fully automatic mode, i.e. the user can just input the SEM images of cBN materials and get the statistical and individual results on image and grain geometry attributes listed in Table 1.

Acknowledgements

We would like to thank members of Powder Metallurgy field of MMC for providing samples.

Disclosure statement

No potential conflict of interest was reported by the author(s).

ORCID

Dmitry S. Bulgarevich http://orcid.org/0000-0002-7086-8396

References

[1] Paredes-Orta CA, Mendiola-Santibañez JD, Manriquez-Guerrero F, et al. Method for grain size determination in carbon steels based on the ultimate opening. Measurement. 2019;133:193–207. doi: 10.1016/j.measurement.2018.09.068

[2] Oguchi S, Yumoto K, Miyashita Y. CBN sintered compact with fine ceramics binder. In: An International Technical Conference on Diamond, Cubic Boron Nitride and their Applications; 2015 May 19–20 May; (IN)polis, (IN), USA. Curran Associates, Inc.; 2016. https://www.proceedings.com/content/028/028237webtoc.pdf

[3] Eko A, Fukunaga O, Ohtake N. High pressure sintering of cubic boron nitride using Co-V-Al alloy as bonding media. Int J Refract Hard Met. 2015;50:178–183. doi: 10.1016/j.ijrmhm.2015.01.007

[4] OLYMPUS Stream software: Count and Measure Solution. Available from: https://www.olympus-ims.com/en/microscope/stream2/#!cms[focus]=cmsContent13576

[5] NIS-Elements Imaging Software. Available from: https://downloads.microscope.healthcare.nikon.com/phase4/literature/Brochures/NIS-Elements_2CE-MPCJ-4_2022-06-30-224308tnya.pdf

[6] Grain Size Analysis and Evaluation. Available from: https://www.keyence.com/ss/products/microscope/vhx-casestudy/automobile/grain-size.jsp

[7] LAS/LAS X Grain Expert software. Available from: https://www.leica-microsystems.com/science-lab/how-to-adapt-grain-size-analysis-of-metallic-alloys-to-your-needs/

[8] Park C, Ding Y. Automating material image analysis for material discovery. MRS Commun. 2019;9(2):545–555. doi: 10.1557/mrc.2019.48

[9] Miyazaki S, Kusano M, Bulgarevich DS, et al. Image segmentation and analysis for microstructure and property evaluations on Ti–6Al–4V fabricated by selective laser melting. Mater Trans. 2019;60(4):561–568. doi: 10.2320/matertrans.MBW201806

[10] Kusano M, Miyazaki S, Watanabe M, et al. Tensile properties prediction by multiple linear regression analysis for selective laser melted and post heat-treated Ti-6Al-4V with microstructural quantification. Mater Sci Eng A. 2020;787:139549–10. doi: 10.1016/j.msea.2020.139549

[11] Nock R, Nielsen F. Statistical region merging. IEEE Trans Pattern Anal Mach Intell. 2004;26(11):1452–1458. doi: 10.1109/TPAMI.2004.110

[12] Legland D, Arganda-Carreras I, Andrey P. MorphoLibJ: integrated library and plugins for mathematical morphology with ImageJ. Bioinformatics. 2016;32(22):3532–3534. doi: 10.1093/bioinformatics/btw413

[13] Münch B, Gasser P, Holzer L. Fib-nanotomography of particulate systems—part II: particle recognition and effect of boundary truncation. J Am Ceram Soc. 2006;89(8):2586–2595. doi: 10.1111/j.1551-2916.2006.01121.x

[14] Schneider CA, Rasband WS, Eliceiri KW. NIH image to ImageJ: 25 years of image analysis. Nat Methods. 2012;9(7):671–675. doi: 10.1038/nmeth.2089

[15] Collins TJ. ImageJ for microscopy. Biotechniques. 2007;43(sup1):S25–S30. doi: 10.2144/000112517

[16] Schindelin J, Arganda-Carreras I, Frise E, et al. Fiji: an open-source platform for biological-image analysis.

Nat Methods. 2012;9(7):676–682. doi: 10.1038/nmeth.2019
[17] Ferreira T, Rasband W. ImageJ user guide IJ 1.46r. 2012. p. 198. Available from: http://imagej.nih.gov/ij/docs/guide
[18] Canny Edge. Available from: https://imagej.net/plugins/xlib/#canny-edge
[19] Find Connected Regions. Available from: https://www.longair.net/edinburgh/imagej/find-connected-regions/
[20] Statistical Region Merging. Available from: https://imagej.net/Statistical_Region_Merging
[21] Xlib. Disconnect particles. Available from: https://imagej.net/plugins/xlib#disconnect-particles
[22] Vincent L, Soille P. Watersheds in digital spaces: an efficient algorithm based on immersion simulation. IEEE Trans Pattern Anal Mach Intell. 1991;13(6):583–598. doi: 10.1109/34.87344
[23] Fauzi Ismail NH, Zaini TRM, Jaafar M, et al. H-minima transform for segmentation of structured surface. MATEC Web Conf. 2016;74:00025–6. doi: 10.1051/matecconf/20167400025
[24] Morphological Segmentation. Available from: https://imagej.net/plugins/morphological-segmentation